Matter

Article

Self-floating COF-based Janus film: A robust triphase interface boosting charge separation for efficient H_2O_2 photosynthesis

Graphical abstract

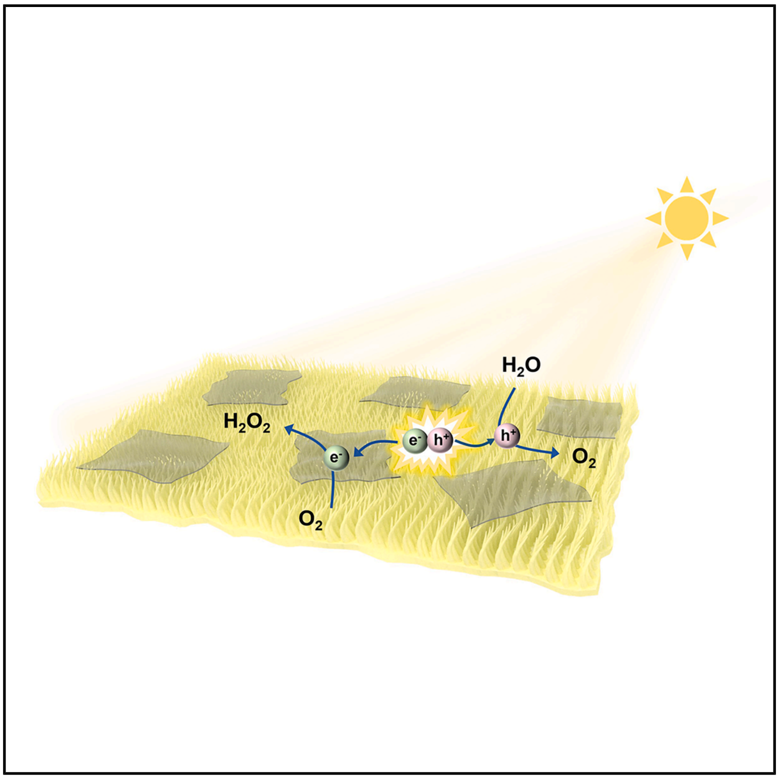

Highlights

- This COF-based Janus film boosts the photogenerated charge separation
- Self-floating film stabilizes the triphase interface for efficient mass transfer
- Photocatalytic film-device shows huge potential in practical applications
- This synthetic approach can be employed in various COFs and nanomaterials

Authors

Ying Li, Yuxin Zhang, Wenjie Shi, ..., Kuo Yuan, Di-chang Zhong, Tongbu Lu

Correspondence

yuankuo@email.tjut.edu.cn (K.Y.),
dczhong@email.tjut.edu.cn (D.-c.Z.)

In brief

A self-floating COF-[NH_2-GO] Janus film was engineered via a one-step interfacial polymerization strategy for efficient H_2O_2 photosynthesis, in which the introduced graphene promoted the separation and transfer of photogenerated carriers. Meanwhile, the self-floating film photocatalysts enabled the stabilization of gas-liquid-solid triphase interface, significantly enhancing the O_2 mass transfer.

5

Improvement

Enhanced performance with innovative design or material control

Li et al., 2026, Matter 9, 102679
May 6, 2026
https://doi.org/10.1016/j.matt.2026.102679

CellPress

Please cite this article in press as: Li et al., Self-floating COF-based Janus film: A robust triphase interface boosting charge separation for efficient H_2O_2 photosynthesis, Matter (2026), https://doi.org/10.1016/j.matt.2026.102679

Matter

CellPress

Article

Self-floating COF-based Janus film: A robust triphase interface boosting charge separation for efficient H_2O_2 photosynthesis

Ying Li,[1,5] Yuxin Zhang,[2,5] Wenjie Shi,[1,5] Chao Zhang,[1,5] Qinbai Yun,[3] Zongyang Liu,[1] Fuli Ye,[2] Jun Guo,[2] Qingle Yuan,[1] Wenqiang Li,[1] Miao Wang,[4] Xiaotao Zhang,[4] Wenping Hu,[4] Kuo Yuan,[1,6,*] Di-chang Zhong,[1,*] and Tongbu Lu[1]

[1]Institute for New Energy Materials and Low Carbon Technologies, School of Materials Science & Engineering, Tianjin University of Technology, Tianjin 300384, China

[2]State Key Laboratory of Advanced Separation Membrane Materials, School of Material Science and Engineering, Tiangong University, Tianjin 300387, P.R. China

[3]Sustainable Energy and Environment Thrust, The Hong Kong University of Science and Technology (Guangzhou), Nansha, Guangzhou 511400, China

[4]Department of Chemistry, School of Science & Key Laboratory of Organic Integrated Circuits, Ministry of Education, Tianjin University, Tianjin 300072, China

[5]These authors contributed equally

[6]Lead contact

*Correspondence: yuankuo@email.tjut.edu.cn (K.Y.), dczhong@email.tjut.edu.cn (D.-c.Z.)

https://doi.org/10.1016/j.matt.2026.102679

PROGRESS AND POTENTIAL Artificial photosynthesis is a promising and sustainable approach for H_2O_2 production. As an emerging photocatalyst material, self-floating film, acting as a robust gas-liquid-solid triphase interface, can address the dilemma of sluggish O_2 mass transport in water for a triphase system. Nevertheless, the precise construction of heterostructures in films is still a huge challenge, causing the shortage of effective regulation over photogenerated charge kinetics. Herein, we present a self-floating COF-[NH_2-GO] film, synergistically optimizing charge kinetics and mass transport in triphase artificial photosynthesis. Hence, the photocatalytic production of H_2O_2 was greatly improved. Furthermore, a film-based device for *E. coli* sterilization was constructed, demonstrating its potential in practical applications. Importantly, this synthetic approach can be extended to other COFs, C_3N_4, and CNT, providing a universal blueprint for designing floating film photocatalyst for different demands.

SUMMARY

H_2O_2 photosynthesis, as a gas-liquid-solid reaction, faces two giant challenges, i.e., charge recombination and sluggish oxygen transport. For improving efficiency, it is a feasible strategy to construct a robust triphase interface with optimized charge kinetics. Herein, we constructed a self-floating covalent-organic framework (COF)-based film with Janus heterostructure, i.e., COF-[NH_2-GO]. In overall H_2O_2 photosynthesis, COF-[NH_2-GO] exhibited the highest yield among COF film and powder, signifying improved separation and transfer of photogenerated carriers. The photocatalytic triphase system achieved 5,306.6 $\mu mol\cdot m^{-2}\cdot h^{-1}$ H_2O_2 yield, higher than that of diphase counterpart, ascribed to the promoted O_2 delivery. It was demonstrated that excellent photocatalytic performance was attributed to the improved charge kinetics and mass transfer. A prototypical film-based device was designed for photosynthesis and collection of H_2O_2, which exhibited bactericidal activity against *Escherichia coli*. More importantly, this strategy could be extended to other COFs and functional nanomaterials. This work provides new insights for challenging triphase photocatalysis.

INTRODUCTION

Hydrogen peroxide (H_2O_2), serving as a green oxidant and sustainable energy carrier, plays an indispensable role in chemical synthesis, wastewater treatment, medical disinfection, and other fields.[1–4] However, conventional industrial production methods (e.g., the anthraquinone process and thermal catalytic synthesis from H_2/O_2) suffer from intrinsic drawbacks, e.g., high energy consumption, complex processes, and safety risks.[5–8] In contrast, artificial photosynthesis utilizes solar energy to directly

Please cite this article in press as: Li et al., Self-floating COF-based Janus film: A robust triphase interface boosting charge separation for efficient H_2O_2 photosynthesis, Matter (2026), https://doi.org/10.1016/j.matt.2026.102679

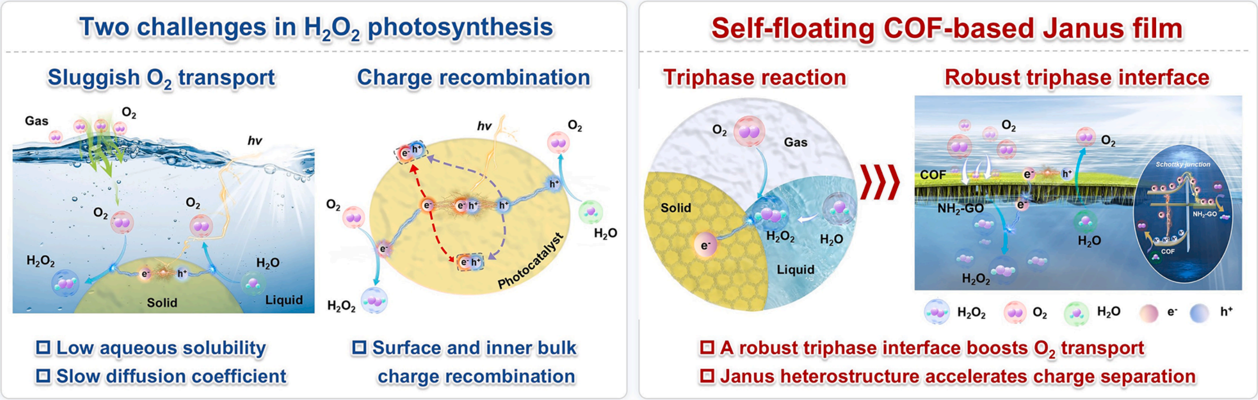

Scheme 1. Design principles and challenges for triphase photocatalytic H_2O_2 production

produce H_2O_2 from water and oxygen, and hence is regarded as an ideal and green approach owing to its eco-friendly advantage.[9–13] Photocatalytic synthesis of H_2O_2 primarily proceeds through two fundamental pathways—the oxygen reduction reaction (ORR) and the water oxidation reaction (WOR).[14–16] Due to the harsh conditions required for WOR, the two-electron ORR is currently one of central pathways for H_2O_2 photosynthesis.[17–20] Essentially, ORR process is a triphase reaction, which involves gaseous O_2, liquid water, and solid photocatalysts. However, most of conventional photocatalytic systems are based on a liquid-solid diphase system, where the photocatalytic activity is significantly limited by the low aqueous solubility (8 $mg \cdot L^{-1}$ at 25°C) and a slow diffusion coefficient (2.10×10^{-9} $m^2 \cdot s^{-1}$) of O_2 (scheme 1).[21] In contrast, the O_2 diffusion rate in air of the gas-liquid-solid triphase system is approximately 10,000 times higher than that of a diphase system, signifying more ample supply of O_2 for H_2O_2 production.[22]

The superior O_2 mass transfer capability in triphase systems highlights the importance of gas-liquid-solid interface properties in photocatalytic H_2O_2 production. Various strategies have been developed to facilitate O_2 access to the catalyst surface (Figure S1). As one of the most common approaches, physical stirring was driven by external force to promote the contact between O_2 and catalyst, which requires continuous and extensive energy consumption.[23] In addition, light scattering in the suspension influences the light harvesting of photocatalysts, hindering the photocatalytic performance.[24] To circumvent these problems, some researchers have developed support photocatalysts on hydrophobic substrates to construct a triphase system. The stable gas-liquid-solid interface significantly accelerates gas diffusion and thereby boosts photocatalytic activity.[25,26] However, these supported floating photocatalysts present several challenges, including catalyst detachment and blockage of active sites, which severely threaten both photocatalytic activity and stability.[27] Therefore, in order to address the aforementioned challenges, it is significant and urgent to develop self-floating film photocatalysts without additional substrates.

In recent decades, covalent organic frameworks (COFs), featuring high specific surface areas, regulable energy levels, tailorable frameworks, excellent stability, and pronounced light responsiveness, have emerged as promising photocatalysts.[28–36] Compared with powder samples, COF films possess some unique advantages such as low light scattering, excellent scalability, easy recyclability, facile device integration, and sufficient contact with reactants, making them a highly sought-after platform for artificial photosynthesis.[37–39] Various strategies have been extensively investigated to construct COF films, e.g., interfacial polymerization,[40,41] vapor-assisted conversion,[42] and *in situ* solvothermal[43,44] approaches. Among these, the liquid-liquid interfacial polymerization method has attracted significant attention due to its simple process and ability to produce high-quality films under mild conditions. The stable oil-water interface enables precise control over monomer diffusion and reaction kinetics, which is favorable for synthesizing continuous, uniform, and free-standing COF films.[45] Unfortunately, the photocatalytic performance of pristine COF films is limited by the rapid recombination of photogenerated electron-hole pairs and lack of active sites[46,47] (scheme 1). Notably, as for powder photocatalysts, COF-based composite materials have been developed to address these dilemmas by constructing various heterojunctions, such as semiconductor-semiconductor[48–50] and semiconductor-metal composites.[51] Therefore, engineering heterostructures in COF films is regarded as a feasible and promising approach for enhancing the overall photocatalytic activity. However, the self-floating COF film with programmable heterojunctions is still rarely reported.

Herein, we present a one-step interfacial polymerization approach to construct a self-floating Janus film photocatalyst COF-[NH_2-GO] (scheme 1). Under pure water and open air without any sacrificial agents, H_2O_2 yield of COF-[NH_2-GO] film reached 922.10 $\mu mol \cdot g^{-1} \cdot h^{-1}$, which was around 1.44-fold higher than that of COF film (638.70 $\mu mol \cdot g^{-1} \cdot h^{-1}$) and 4.54-fold higher than that of COF powder (203.30 $\mu mol \cdot g^{-1} \cdot h^{-1}$). Based on spectral characterizations, it was demonstrated that the introduced graphene effectively facilitated the separation of photogenerated carriers, thereby enhancing the photocatalytic performance. Furthermore, the areal activity of COF-[NH_2-GO] film in the triphase system reached 3145.80 $\mu mol \cdot m^{-2} \cdot h^{-1}$, representing a 2.36-fold enhancement compared with the diphase system. Numerical simulations confirmed that a relatively high

O_2 concentration was always maintained at the triphase reaction interface, which was conducive to the generation of H_2O_2. Furthermore, a COF-[NH_2-GO] film-based device was constructed for H_2O_2 photosynthesis and collection, enabling effective bactericidal action against *Escherichia coli* (*E. coli*). The methodology has been successfully extended to diverse COFs and functional nanomaterials, all exhibiting substantially enhanced photocatalytic H_2O_2 production, confirming its broad applicability. To our knowledge, our work is the first example of a self-floating COF-based Janus film capable of achieving triphase photocatalytic H_2O_2 production, which not only advances the development of COF-based composite films but also offers a new design paradigm for photocatalytic H_2O_2 generation.

RESULTS AND DISCUSSION

Material synthesis and characterization

Owing to the extended π-conjugated framework, triazine-based COF materials exhibit remarkable visible light-harvesting capabilities.[52] Besides, imine-linked COFs could be synthesized at room temperature.[53,54] Therefore, we employed 2,4,6-tris(4-aminophenyl)-1,3,5-triazine (TTA) and 2,4,6-tris(4-formylphenyl)-1,3,5-triazine (TTB) as building blocks for the *in situ* construction of COF films at the liquid-liquid interface. TTB was dissolved in dichloromethane (DCM) as the oil phase at bottom. A small amount of water was then introduced on the oil surface as a buffer layer, into which an acetic acid aqueous solution containing TTA was carefully added. The as-prepared diphase system was kept undisturbed at room temperature for 7 days, after which a yellow film formed at the liquid-liquid interface. After reaction, the upper aqueous layer was removed, and the synthesized COF film was collected and washed. As shown in Figure S2, the optical photograph showed that the COF film suspended on a metal wire loop was uniform and intact, signifying its self-supporting property. Scanning electron microscopy (SEM) images showed that the top surface (water phase) of the COF film was interweaved networks with elongated fibrous structures (Figure S3A). In contrast, the bottom surface of the film (oil phase) displayed a uniformly packed granular structure without obvious gaps (Figure S3B). The water contact angles of top and bottom surfaces of the COF film were 21.5° and 58.8°, respectively (Figure S4). The difference in surface wettability between the two sides of the COF film signified an asymmetric structure. Cross-sectional SEM image indicated a uniform thickness of approximately 8 μm (Figure S3C). High-resolution transmission electron microscopy (HRTEM) images revealed clear lattice fringes of the COF film with a spacing of approximately 2.0 nm, corresponding to the (100) crystal facet, which indicated good crystallinity (Figure S5). To further determine the crystalline structure, X-ray diffraction (XRD) was conducted on the COF film. The characterized peaks at 4.0°, 7.1°, 8.2°, and 10.8° corresponded to the (100), (110), (200), and (120) crystal faces, respectively, which were consistent with those of the simulated one (Figure S6). For comparison, the corresponding COF powder was synthesized via a solvothermal method. XRD and Fourier transform infrared (FTIR) spectroscopy confirmed the successful preparation of COF powder (Figures S6 and S7). SEM image of the powder sample showed a loose morphology, while HRTEM observations clearly indicated lattice fringes (Figures S8 and S9).

Given that the charge separation efficiency plays an important role in photocatalytic performance, graphene with superior electrical conductivity was selected as the functional unit to be integrated into COF films. In order to optimize the interaction between COF and graphene, NH_2 groups were grafted on the surface of graphene oxide to prepare NH_2-functionalized graphene oxide (NH_2-GO), via a covalent bonding strategy between anchoring (3-aminopropyl) triethoxysilane (APTS) and graphene oxide (GO) (Figure S10). Compared with GO, FTIR spectra of NH_2-GO (Figure S11) showed new peaks at 2951, 1634, and 1125 cm^{-1}, assigned to the stretching vibrations of C-H, N-H, and Si-O-C bonds, respectively, which confirmed the successful incorporation of APTS onto GO. Transmission electron microscope (TEM) image showed the maintained nanosheet morphology of NH_2-GO (Figure S12A). Furthermore, energy dispersive X-ray spectroscopy (EDS) elemental mapping of NH_2-GO showed a uniform distribution of C, N, O, and Si (Figures S12B–S12F). These results confirmed that the surface of GO was successfully decorated by amino functional groups.

The as-prepared NH_2-GO was employed in the liquid-liquid interfacial approach to directly construct COF-[NH_2-GO] composite film. This was achieved by simply replacing the buffer water layer with an aqueous dispersion of NH_2-GO, while keeping all other steps unchanged (Figure 1A). The as-prepared COF-[NH_2-GO] film exhibited excellent and stable self-floating ability, which was crucial for stabilizing the gas-liquid-solid triphase interface during photocatalysis. As shown in Figures 1B and S13, the film could stably float on water. Under static conditions, this composite film could float on water surface for over one month without sinking. As shown in Figure S14 and Videos S1 and S2, this self-floating COF-[NH_2-GO] film could remain stable on the water surface, even under vigorous stirring (400 rpm), which was closely correlated with the film's excellent mechanical properties and hydrophobicity. As shown in Figure 1C, the continuous and intact film could be transferred onto a metal wire loop, demonstrating its superior self-supporting property. Moreover, the stable liquid-liquid interface guaranteed the large-scale synthesis of COF and COF-[NH_2-GO] films with a lateral size of 5 cm (Figure S15). The surface morphology and microstructure of the COF-[NH_2-GO] film was further investigated by SEM. The SEM images showed that on the top surface, two-dimensional graphene sheets were uniformly distributed and intertwined with the fibrous network of COF, forming a tightly integrated structure (Figures 1A and S16A). This morphological feature was further corroborated by the cross-sectional SEM image (Figure 1A), confirming the successful incorporation of NH_2-GO and its strong interfacial integration into the COF matrix. In contrast, the bottom surface of the COF-[NH_2-GO] film consisted of uniformly packed granular architecture similar to the COF film (Figure S16B). Notably, the COF-[NH_2-GO] film demonstrated enhanced hydrophilicity, with the decrease in top surface contact angle to 12° (Figure S17). Overall, it was demonstrated that the COF-[NH_2-GO] film possessed an asymmetric Janus-type structure.

To further investigate the film crystallinity, XRD and HRTEM were employed to characterize the COF-[NH_2-GO] Janus film. As

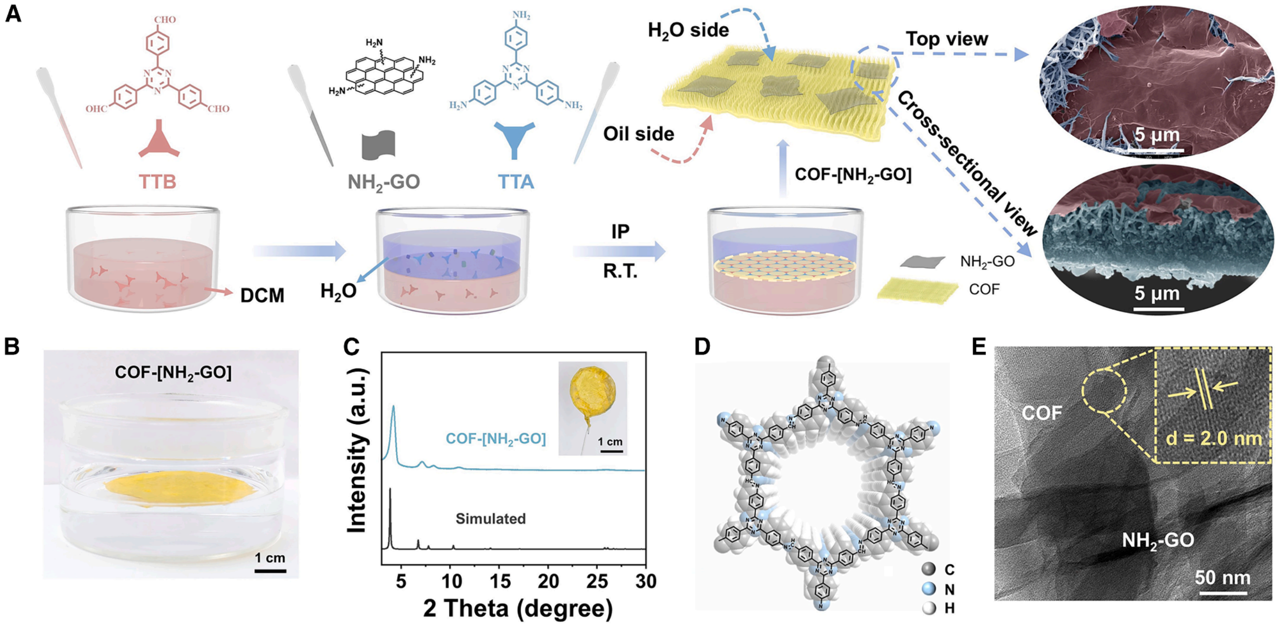

Figure 1. Synthesis and characterizations of the COF-[NH_2-GO] Janus film

(A) Synthesis process of the COF-[NH_2-GO] film, and SEM images of the top surface (in H_2O phase) and cross-section of the COF-[NH_2-GO] film (DCM: dichloromethane; GO: graphene oxide; TTB, 2,4,6-tris(4-formylphenyl)-1,3,5-triazine; and TTA, 2,4,6-tris(4-aminophenyl)-1,3,5-triazine).

(B) Optical photograph of as-prepared COF-[NH_2-GO] film floating on the water surface. Scale bar, 1 cm.

(C) XRD profiles of the COF-[NH_2-GO] film and the simulation result.

(D) The structure of COF based on TTB and TTA.

(E) HRTEM image of the COF-[NH_2-GO] film.

XRD, X-ray diffraction; HRTEM, high-resolution transmission electron microscopy.

shown in Figures 1C and 1D, the XRD pattern of COF-[NH_2-GO] composite film exhibited characteristic peaks corresponding to the COF component, confirming the crystalline structure of the COF within composite films. HRTEM image of the COF-[NH_2-GO] film not only revealed the integration of COF and NH_2-GO but also showed that the crystal fringe of COF was approximately 2.0 nm (Figure 1E). This spacing corresponded to the (100) crystal facet and was consistent with that of the COF film, further verifying the crystalline structure of COF in the composite films. In addition, EDS elemental mapping of COF-[NH_2-GO] film showed the uniform distribution of C, N, O, and Si (Figure S18), further revealing the successful integration COF and NH_2-GO in the composite films. FTIR spectra of the COF-[NH_2-GO] film exhibited a new characteristic peak of imine stretching vibration at 1,628 cm^{-1}, confirming the formation of imine bond within the composite material (Figure S19). The porosity of COF-[NH_2-GO] and COF films was evaluated by N_2 sorption isotherms measured at 77 K. As shown in Figure S20, the specific surface area of the COF film was 749.89 $m^2 \cdot g^{-1}$, and after the incorporation of NH_2-GO, the specific surface area of COF-[NH_2-GO] film slightly decreased to 530.18 $m^2 \cdot g^{-1}$. Thermogravimetric analysis (TG) results demonstrated that both COF and COF-[NH_2-GO] films possessed excellent thermal stability (Figure S21). The above-mentioned results all demonstrated the successful preparation of COF-[NH_2-GO] Janus film.

As a kind of semiconductor material, the band structure of COF should be determined. UV-Vis diffuse reflectance spectroscopy (UV-vis DRS) was employed to characterize the light capturing ability of COF. As shown in Figure 2A, the COF film exhibited pronounced absorption in the visible region. The incorporation of NH_2-GO significantly enhanced the absorption intensity and induced a distinct red-shift in the absorption edge, indicating improved visible light utilization. The optical band gap (Eg) of COF was determined to be 2.45 eV by Tauc plot analysis (Figure S22A), while the Mott-Schottky measurement result (Figure S22B) showed that the conduction band (CB) position of COF was −0.76 V relative to normal hydrogen electrode (NHE). Afterward, the valence band (VB) position was calculated to be 1.69 V. This band structure of COF film was thermodynamically feasible for the photocatalytic reduction of O_2 to H_2O_2 and the oxidation of H_2O to O_2. Furthermore, ultraviolet photoelectron spectroscopy (UPS) measurements determined work function values of 5.35 eV and 5.47 eV for COF and NH_2-GO, respectively (Figure S23). The higher Fermi level of COF relative to NH_2-GO prompted electron transfer from COF to NH_2-GO upon contact until equilibrium was reached. Within this configuration, photoexcited electrons were preferentially injected into the conductive NH_2-GO domains, which served as electron collectors and facilitated the adsorption and activation of O_2 molecules. Thus, NH_2-GO could act as a charge mediator to promote charge separation and interfacial electron transfer from COF to NH_2-GO (Figure 2B).

Photocatalytic H_2O_2 performance

Given the light-capturing capability and band structures of COF and graphene, the COF and COF-[NH_2-GO] Janus films were

Please cite this article in press as: Li et al., Self-floating COF-based Janus film: A robust triphase interface boosting charge separation for efficient H_2O_2 photosynthesis, Matter (2026), https://doi.org/10.1016/j.matt.2026.102679

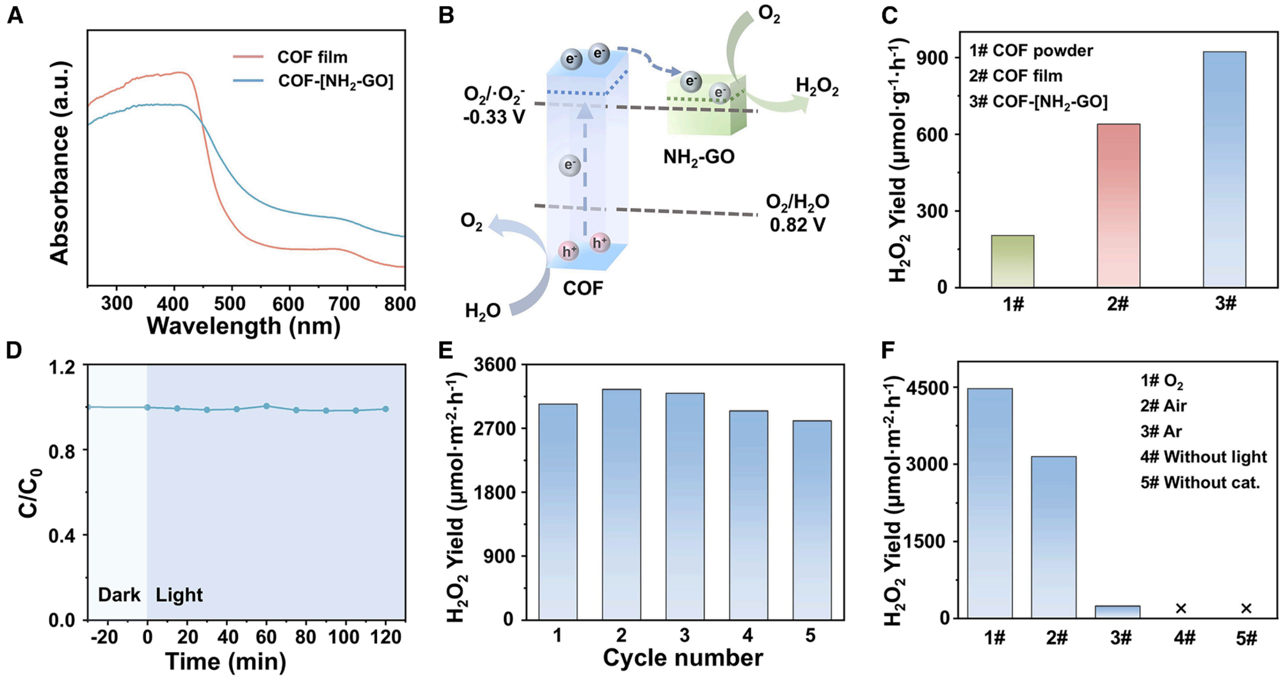

Figure 2. Photocatalytic experiments for powder and film samples

(A) UV-vis spectra of the COF and COF-[NH_2-GO] films.

(B) Band structure of the COF-[NH_2-GO] film.

(C) Photocatalytic mass-activity of COF powder, COF film, and COF-[NH_2-GO] film for the photosynthesis of H_2O_2.

(D) H_2O_2 (100 μM) degradation study for the COF-[NH_2-GO] film under dark and illumination in Ar atmosphere.

(E) Cycling experiments of the COF-[NH_2-GO] film for the photosynthesis of H_2O_2.

(F) Control experiments of the COF-[NH_2-GO] film for the photosynthesis of H_2O_2.

placed in an air-water system to evaluate their photocatalytic performance for H_2O_2 synthesis under visible light ($\lambda > 420$ nm, 100 mW cm^{-2}) without any sacrificial agents. The concentration of the generated H_2O_2 was quantified using iodometry colorimetry (Figure S24). As shown in Figure 2C and Table S1, the photocatalytic H_2O_2 production rate over COF-[NH_2-GO] film reached 922.10 $\mu mol \cdot g^{-1} \cdot h^{-1}$, which was 1.44- and 4.54-fold higher than that of COF film and COF powder, respectively. This enhancement suggested that the incorporation of GO facilitated the separation and transfer of photogenerated carriers, thereby improving the photocatalytic activity for H_2O_2 synthesis. Notably, the areal activity of COF-[NH_2-GO] film attained 3145.80 $\mu mol \cdot m^{-2} \cdot h^{-1}$. In comparison with previous COF-based photocatalysts, the as-synthesized COF-[NH_2-GO] film exhibited excellent photocatalytic activity (Table S2). Due to the poor stability of H_2O_2, the degradation in the presence of the COF-[NH_2-GO] and COF films was investigated under both dark and illuminated conditions. As shown in Figure 2D, the concentration of H_2O_2 remained nearly constant under both dark and illuminated conditions, indicating that neither the presence of the catalyst nor the illumination process exerted a significant effect on the decomposition of H_2O_2. Furthermore, the COF-[NH_2-GO] film demonstrated excellent stability in the photocatalytic production of H_2O_2. Even after five consecutive catalytic cycles, the yield of H_2O_2 showed no significant decline (Figure 2E; Table S3), which attested to the high photostability and reusability of the catalyst. After the photocatalytic reaction, the COF-[NH_2-GO] film still floated on water surface and maintained whole integrity without cracking (Figure S25), certifying the stable gas-solid-liquid triphase interface. In addition, the used COF-[NH_2-GO] film was further confirmed by XRD, HRTEM, FTIR, and SEM images (Figures S26–S29), revealing that its crystalline phase, composition, and morphology could be maintained after the photocatalytic process. Furthermore, the photocatalytic performance of the COF-[NH_2-GO] film for H_2O_2 production was evaluated under natural sunlight. As shown in Figure S30 and Table S4, the H_2O_2 yield achieved approximately 2,500.00 $\mu mol \cdot m^{-2} \cdot h^{-1}$ under solar illumination. Furthermore, the COF-[NH_2-GO] film showed excellent photocatalytic H_2O_2 yields in lake water (2931.1 $\mu mol \cdot m^{-2} \cdot h^{-1}$) and seawater (2850.6 $\mu mol \cdot m^{-2} \cdot h^{-1}$), as shown in Figure S31 and Table S5. These results further demonstrated the practical applicability of the COF-[NH_2-GO] film and underscored its potential for practical solar-driven synthesis of H_2O_2. The photocatalytic generation of H_2O_2 over the COF-[NH_2-GO] film was explored through a series of control experiments to investigate the reaction process of H_2O_2 production. As shown in Figure 2F and Table S6, H_2O_2 formation was not observed in the absence of either COF-[NH_2-GO] film or light irradiation, confirming that both the photocatalyst and light were essential for the reaction. H_2O_2 was hardly detectable under an argon atmosphere, while an oxygen atmosphere led to a higher yield compared to air, indicating that oxygen participated in H_2O_2 photosynthesis.

Please cite this article in press as: Li et al., Self-floating COF-based Janus film: A robust triphase interface boosting charge separation for efficient H_2O_2 photosynthesis, Matter (2026), https://doi.org/10.1016/j.matt.2026.102679

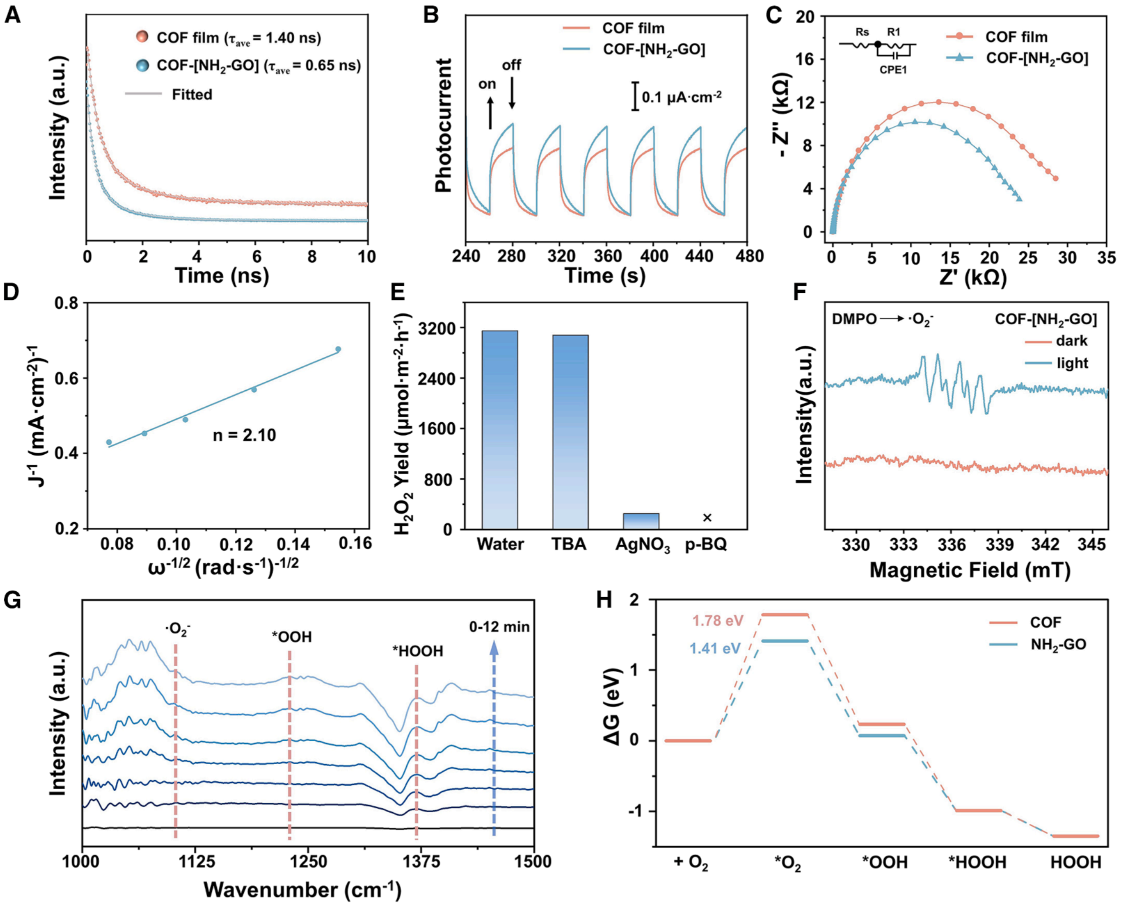

Figure 3. Mechanistic investigation for photocatalytic H_2O_2 production

(A–C) TRPL spectra (excitation wavelength: 375 nm), photocurrent measurements, and EIS Nyquist plots of the COF and COF-[NH_2-GO] films.

(D) Koutecky-Levich plot of the COF-[NH_2-GO] film obtained via RDE measurement in phosphate buffer solution (pH = 7) with continuous O_2 purging.

(E) Photocatalytic activity of COF-[NH_2-GO] film for synthesizing H_2O_2 in the presence of TBA (10 mM), $AgNO_3$ (10 mM), or p-BQ (10 mM).

(F) EPR spectra of COF-[NH_2]-GO film in the presence of DMPO.

(G) *In situ* FTIR spectra of COF-[NH_2-GO] film in H_2O_2 photosynthesis.

(H) Free energy diagrams of photocatalytic O_2 reduction pathways on COF and NH_2-GO within COF-[NH_2-GO] film.

TRPL, time-resolved photoluminescence; RDE, rotating disk electrode; EPR, electron paramagnetic resonance; and FTIR, Fourier transform infrared.

The exceptional photocatalytic performance of the COF-[NH_2-GO] film in H_2O_2 photosynthesis prompted a detailed investigation into the kinetics of photogenerated carriers. Photoluminescence (PL) spectroscopy showed that the fluorescence intensity of COF-[NH_2-GO] was lower than that of COF (Figure S32), indicating that the recombination of photogenerated electrons and holes was significantly suppressed. In addition, time-resolved photoluminescence (TRPL) spectroscopy revealed that the average exciton lifetime of the COF-[NH_2-GO] film was 0.65 ns, lower than that of the COF film (1.40 ns), suggesting that the introduced NH_2-GO significantly accelerated charge transfer (Figure 3A and Table S7). In the photocurrent measurement, the photocurrent density of the COF-[NH_2-GO] film was higher than that of the COF film (Figure 3B), indicating a faster charge transfer rate in the COF-[NH_2-GO] film. Moreover, electrochemical impedance spectroscopy (EIS) was employed to evaluate the charge kinetics. As shown in Figure 3C, the semicircle radius in the Nyquist plot of the COF-[NH_2-GO] film was significantly smaller than that of the COF film, which indicated that the grafting of graphene onto COF indeed promoted charge transfer. In summary, all the above lines of evidence suggested that the introduction of graphene helped improve the separation of photogenerated electrons and holes, thereby achieving more efficient photocatalysis.

Photocatalytic mechanism investigation

To elucidate the mechanism of photocatalytic H_2O_2 production, linear sweep voltammetry (LSV) curves were measured using a rotating disk electrode (RDE), and the electron transfer number (n) involved in the ORR was calculated. Based on the LSV results (Figures 3D, S33, and S34), the Koutecky-Levich (K-L) plots yielded *n* values of 2.1 and 1.5 for the COF-[NH_2-GO] film and the COF film, respectively. It was indicated that the ORR process over these two films followed a two-electron reduction pathway.

Please cite this article in press as: Li et al., Self-floating COF-based Janus film: A robust triphase interface boosting charge separation for efficient H_2O_2 photosynthesis, Matter (2026), https://doi.org/10.1016/j.matt.2026.102679

Moreover, the *n* value of the COF-[NH_2-GO] film was closer to 2 compared with that of the COF film, suggesting improved selectivity toward the two-electron O_2 reduction after the introduction of GO units. In order to further clarify the reaction pathway and identify the active species involved in the $2e^-$ ORR process, quenching experiments were performed using silver nitrate ($AgNO_3$), tert-butano (TBA), and *p*-benzoquinone (p-BQ) as scavengers for photogenerated electrons (e^-), hydroxyl radicals (·OH), and superoxide radicals ($\cdot O_2^-$), respectively (Figure 3E and Table S8). The introduction of $AgNO_3$ resulted in a significant suppression of the H_2O_2 production rate, confirming that photogenerated electrons were essential for reducing O_2 to H_2O_2. In contrast, the presence of TBA caused only a marginal variation in the H_2O_2 yield, ruling out the involvement of ·OH radicals. Most notably, the addition of p-BQ led to a drastic decline in H_2O_2 formation, highlighting the critical role of $\cdot O_2^-$ as a key intermediate and corroborating the $2e^-$ two-step ORR mechanism. Furthermore, electron paramagnetic resonance (EPR) spectroscopy was employed with 5,5-dimethyl-1-pyrroline N-oxide (DMPO) as a spin-trapping agent to verify the presence of$\cdot O_2^-$. Under light irradiation, the EPR spectra of the COF-[NH_2-GO] film exhibited distinct DMPO-$\cdot O_2^-$ signals (Figure 3F), further supporting that the system predominantly followed an indirect $2e^-$ two-step ORR pathway. It was worth noting that the COF-[NH_2-GO] film produced more $\cdot O_2^-$ than the COF film (Figures 3F and S35), indicating more efficient charge separation and transfer within the composite film. Additionally, an isotopic labeling experiment was conducted using $H_2{}^{18}O$ (m/z = 20), instead of H_2O, and the products were analyzed by mass spectrometry. As shown in Figure S36, the peak observed at m/z = 36 could be attributed to $^{18}O_2$, confirming that the evolved O_2 originated from water oxidation. This result indicated that water was preferentially oxidized to oxygen via a four-electron water oxidation pathway ($2H_2O \rightarrow O_2 + 4H^+ + 4e^-$) in the COF-[$NH_2$-GO] film.

In situ FTIR measurement was conducted to monitor the key intermediate species during the ORR process. As illustrated in Figure 3G, the characteristic peaks of $\cdot O_2^-$ (1106 cm^{-1}), *OOH (1229 cm^{-1}), and *HOOH (1370 cm^{-1}) were observed, and their intensities increased gradually with prolonged irradiation time. The detection of$\cdot O_2^-$ intermediate further confirmed that H_2O_2 production over the COF-[NH_2-GO] film occurred via the indirect $2e^-$ two-step ORR mechanism. In addition, density functional theory (DFT) calculations were performed to evaluate free energy changes of the photocatalytic $2e^-$ ORR on both COF and NH_2-GO, aiming to identify the preferential sites for O_2 reduction within the composite material (Figures S37 and S38; Table S16). The reaction pathways were assessed based on four essential steps toward H_2O_2 formation: initial oxygen adsorption onto the catalyst surface forming $*O_2$, the protonation of $*O_2$ to generate *OOH, further protonation of *OOH to form *HOOH, and *HOOH desorption from the catalyst to yield H_2O_2. As shown in Figure 3H, NH_2-GO exhibited a lower free energy change (ΔG) for the formation of $*O_2$ (1.41 eV) than COF (1.78 eV), demonstrating its superior capability in oxygen adsorption and activation. Furthermore, the ΔG value associated with the conversion of $*O_2$ to *OOH was also lower on NH_2-GO, which facilitated the progression of subsequent reaction steps. Therefore, the photocatalytic ORR for H_2O_2 generation that occurs on NH_2-GO was thermodynamically more favorable. This result is consistent with those of previously published studies.[55,56]

Numerical simulations

The photocatalytic production of H_2O_2 is a complicated process at the gas-liquid-solid triphase interface, wherein the oxygen delivery is an important limiting factor. The as-synthesized floating film could effectively stabilize the gas-liquid-solid triphase interface as the catalyzing platform for H_2O_2 photosynthesis. To demonstrate the superiority of the triphase system, the photocatalytic performances of the films were evaluated in diphase and triphase systems. As shown in Figure 4A, the COF-[NH_2-GO] Janus film submerged at the bottom of the reactor was recognized as a diphase system, whereas the COF-[NH_2-GO] film floating on water surface was defined as a triphase system. The photocatalytic reaction was carried out in pure water under visible light irradiation, using air as the oxygen source. As shown in Figure 4B and Table S9, the H_2O_2 production rate in the triphase system reached 3145.80 $\mu mol \cdot m^{-2} \cdot h^{-1}$, approximately 2.36-fold higher than in the diphase system (1332.79 $\mu mol \cdot m^{-2} \cdot h^{-1}$). This remarkable enhancement in performance could be attributed to the more efficient oxygen mass transport in the triphase system.

At this triphase interface, the local O_2 concentration around the photocatalyst played an important role in optimizing the photocatalytic performance. We conducted numerical simulations using the finite-element method (FEM) and physics-informed neural networks (PINNs) to model the mass transport and concentration distributions for both the diphase and triphase systems. The two approaches gave almost identical results (Tables S10 and S11). In the diphase system, the catalytic layer was situated between two aqueous phases (each 5-mm thick), whereas in the triphase system, it was placed between a gas phase (5 mm) and an aqueous phase (5 mm). Considering oxygen solubility under standard conditions (25°C, 101.3 kPa), the bulk O_2 concentrations for the gas and aqueous phases were set to 8.59 mM and 0.27 mM, respectively. The simulations compared the oxygen transport flux (J_{O2}) at the interface and visualized the resulting steady-state spatial distributions of O_2 and H_2O_2 (Figures 4C–4F). The calculated oxygen fluxes provided direct evidence for the advantage in mass transport for the triphase system. As shown in Figure 4E, the total O_2 flux in the triphase system reached 4.500×10^{-7} mol m^{-2} s^{-1}, significantly higher than that in the diphase system (1.848×10^{-7} mol m^{-2} s^{-1}), with the O_2 flux coming predominantly from the upper surface (the gas phase). This stark contrast unequivocally demonstrated that the direct supply of gaseous O_2 was the dominant and highly efficient pathway for oxygen delivery to the catalytic interface. The different oxygen transport capabilities govern the interfacial concentration distributions (Figures 4C, 4D, and 4F). The simulation results revealed that for the diphase system, a significant depletion of O_2 could be noted near the interface, owing to the limited aqueous diffusion flux. In contrast, for the triphase system, the high flux from the gas phase enabled efficient and continuous replenishment of O_2, thereby maintaining a high concentration at the reaction interface, close to its saturation solubility in water. Furthermore,

Please cite this article in press as: Li et al., Self-floating COF-based Janus film: A robust triphase interface boosting charge separation for efficient H_2O_2 photosynthesis, Matter (2026), https://doi.org/10.1016/j.matt.2026.102679

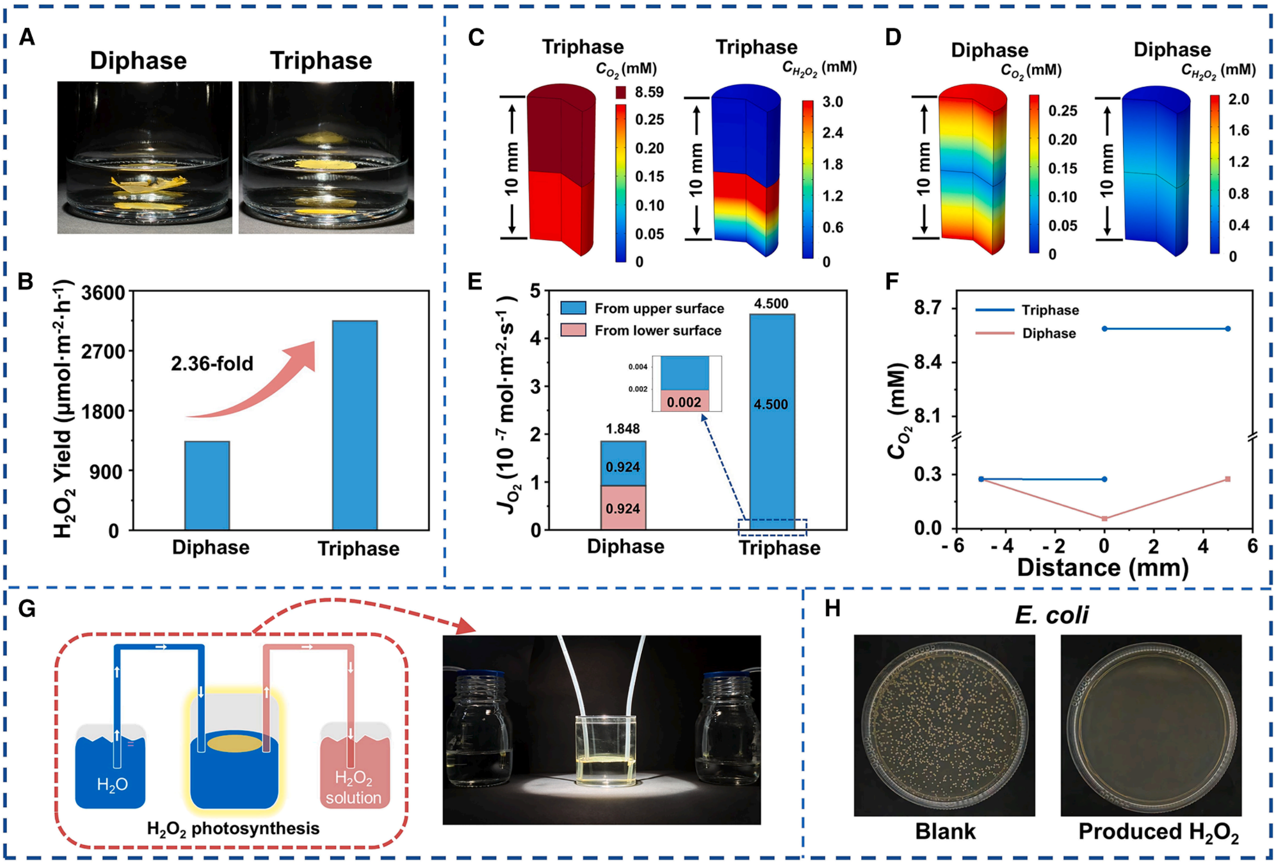

Figure 4. Numerical simulation of the triphase photocatalysis system and practical application

(A) Photographs of the liquid-solid diphase system and the gas-liquid-solid triphase system for the COF-[NH_2-GO] film.

(B) Comparison in terms of photocatalytic activity for the diphase and triphase systems for the COF-[NH_2-GO] film.

(C and D) Comparisons in terms of steady-state distribution of O_2 and H_2O_2 concentrations. (C) Comparison of O_2 and H_2O_2 concentrations for the triphase system. (D) Comparison of O_2 and H_2O_2 concentrations for the diphase system.

(E) Comparison in terms of oxygen transport flux of the triphase and diphase systems.

(F) Oxygen concentration in the triphase and diphase systems, calculated from the diffusion model.

(G) Schematic of the prototypical film-based device for photosynthesis and collection of H_2O_2.

(H) Sterilization of *E. coli* by photosynthesized H_2O_2 over COF-[NH_2-GO] film.

the concentration of H_2O_2 produced in the triphase system reached a maximum of 3.00 mM, considerably higher than that in the diphase system (0.27 mM). These results demonstrated that the rapid transport of O_2 in the triphase configuration was a key factor for enhancing the photocatalytic H_2O_2 production rate. In addition, NH_2-GO was exposed in aqueous solution, and the H_2O_2 yield of the COF-[NH_2-GO] film was 3,145.8 μmol m^{-2} g^{-1} (Figure S39). However, when NH_2-GO was exposed in air, the H_2O_2 yield decreased to 1917.93 μmol m^{-2} g^{-1}. It was confirmed that the orientation mode of the COF-[NH_2-GO] film influenced the photocatalytic performance.

To evaluate its practical potential, a film-based prototypical device was designed and fabricated for the sterilization of *E. coli* (Figure 4G). In this setup, pure water was pumped into a module packed with the COF-[NH_2-GO] film catalyst under visible light irradiation, and the concentration of as-synthesized H_2O_2 solution was about 3 mM. The as-collected solution was subsequently used for antibacterial experiments against *E. coli*. As shown in Figure 4H, the growth of *E. coli* was effectively inhibited when the bacterial culture was co-cultured with a H_2O_2 solution obtained from our photocatalytic system. We further performed numerical simulations to model the dynamics of fluid flow and H_2O_2 transport within the film-based device (Figure S40). These results demonstrated not only the successful photocatalytic production of H_2O_2 in this device but also its strong antibacterial efficacy, highlighting the potential of the system for practical water disinfection applications.

The general strategy for synthesizing COF-based Janus films

To demonstrate the universality of the synthesizing approach for COF-based Janus film, we systematically prepared a series of composite films by varying both COFs or functional nanomaterials. As shown in Figure 5A, three different COFs (including TTA-Tp-COF, TTA-Da-COF, and the original COF) and two types of

Please cite this article in press as: Li et al., Self-floating COF-based Janus film: A robust triphase interface boosting charge separation for efficient H_2O_2 photosynthesis, Matter (2026), https://doi.org/10.1016/j.matt.2026.102679

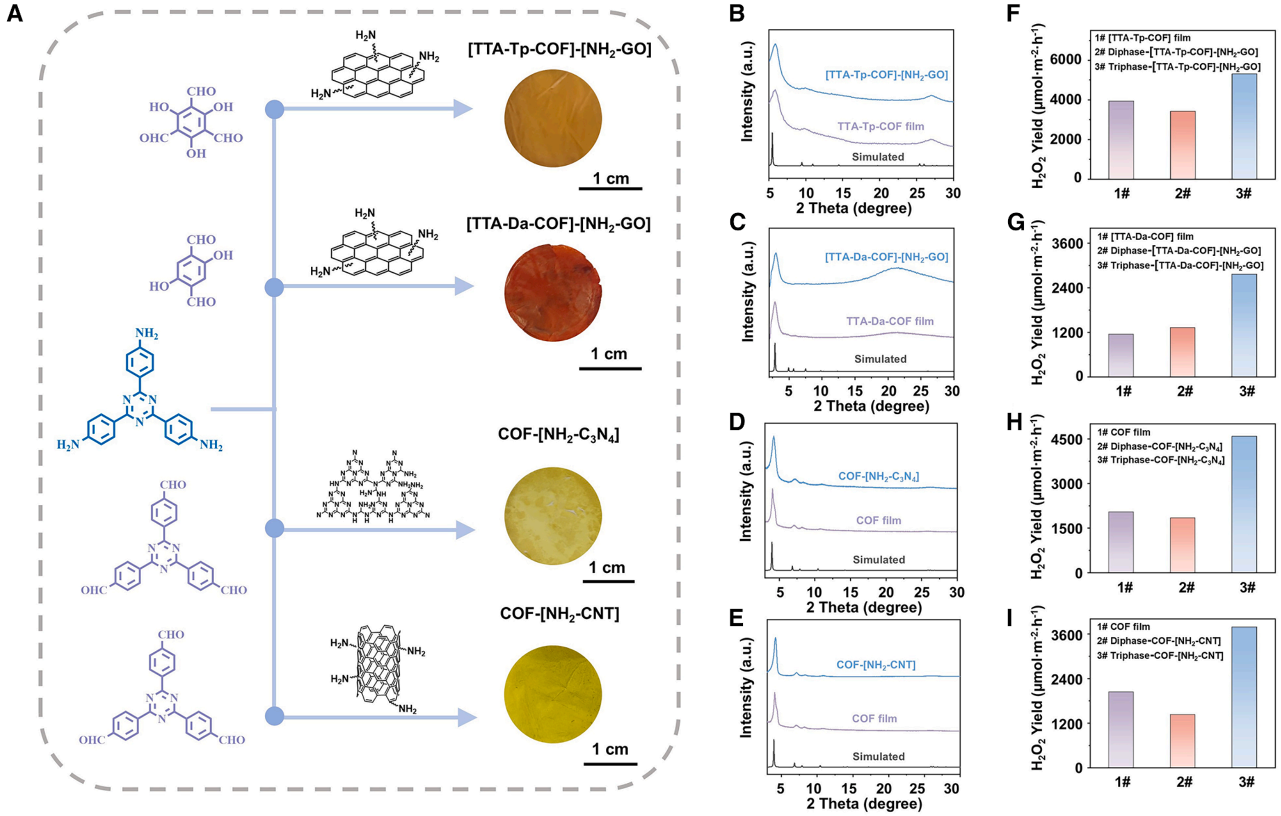

Figure 5. General synthesis strategy for COF-based Janus film

(A) Synthesis and optical photographs of different COF-based Janus films. Scale bar, 1 cm.

(B–E) XRD profiles of COF-based Janus films, COF films, and the corresponding simulation results.

(F–I) Photocatalytic activity of COF films and COF-based Janus films in the diphase and triphase systems for H_2O_2 photosynthesis.

XRD, X-ray diffraction.

functional nanomaterials, namely aminated graphitic carbon nitride (NH_2-C_3N_4) and aminated carbon nanotubes (NH_2-CNT), were employed. As shown in Figures 5A and S41, the corresponding optical photographs showed that all the prepared COF and COF-based composite films were uniform and intact. Contact angle measurements revealed the asymmetry wettability of the two sides for these films. After integrating with functional nanomaterials, the hydrophilicities of top surfaces (in H_2O phase) for these composite films increased to some extent (Figures S42–S47). As shown in Figures S48–S53, the SEM images of these films showed the different morphologies in their top and bottom surfaces, and the functional nanomaterials were uniformly dispersed on the film top surface. The above results show that all combinations successfully yielded COF-based Janus films with well-defined heterostructures. The XRD patterns of four composite films all exhibited diffraction peaks corresponding to COFs, confirming the crystalline structures of COFs in these composite films (Figures 5B–5E). In addition, all composite films showed broadened visible light absorption relative to the pristine COF films (Figures S53–S57). The band gap widths and the VB positions were determined by Tauc diagrams and Mott Schottky measurements, respectively (Figures S58 and S59). Photocatalytic H_2O_2 production tests demonstrated that the self-floating COF-based Janus films in the triphase system achieved the highest H_2O_2 yields (Figures 5F–5I; Tables S12–S15), outperforming both the COF films and the corresponding diphase systems. Among them, the [TTA-Tp-COF]-[NH_2-GO] film delivered the highest H_2O_2 production rate, reaching up to 5,306.6 $\mu mol \cdot m^{-2} \cdot h^{-1}$ (Figure 5F; Tables S10). These results highlighted the consistent synergistic enhancement effect between the COF and functional nanomaterials, as well as the advantage of the self-floating triphase structure. Furthermore, as for all composite films, the smaller half arc in EIS Nyquist plots and higher photocurrent density demonstrated better separation and transfer of photogenerated carriers (Figures S60–S67). In summary, despite variations in either organic or inorganic constituents, all four materials maintained structural integrity while exhibiting consistently improved light absorption, photocatalytic H_2O_2 production, and charge separation behavior. These findings collectively confirmed the universality and superiority of the one-step interfacial polymerization approach for fabricating functional self-floating COF-based Janus film for photocatalytic applications.

Conclusions

In this work, we employed a facile one-step interfacial polymerization strategy to fabricate a self-floating COF-[NH_2-GO] Janus film for H_2O_2 photosynthesis. The introduced graphene in this

Please cite this article in press as: Li et al., Self-floating COF-based Janus film: A robust triphase interface boosting charge separation for efficient H_2O_2 photosynthesis, Matter (2026), https://doi.org/10.1016/j.matt.2026.102679

unique heterostructure effectively promoted the separation and transfer of photogenerated carriers, while the self-floating film photocatalysts stabilized the gas-liquid-solid triphase interface to significantly enhance O_2 mass transfer. These factors collectively boosted the photocatalytic production of H_2O_2. Moreover, the practical applicability of the film was demonstrated by designing a film-based device capable of continuously generating H_2O_2 for the sterilization of *E. coli*. Importantly, the generality of interfacial assembly strategy for fabricating COF-based Janus films was verified through its successful extension to other COF frameworks and functional nanomaterials (i.e., C_3N_4 and CNT). This work not only presents a prospect for triphase artificial photosynthesis (e.g., H_2O_2 synthesis, CO_2 reduction, nitrogen fixation, and organic pollutant degradation) but also offers an insightful paradigm for designing advanced functional composite films.

METHODS

Materials

2,4,6-tris(4-formylphenyl)-1,3,5-triazine (TTB, $C_{24}H_{15}N_3O_3$, 97%), 2,4,6-tris(4-aminophenyl)-1,3,5-triazine (TTA, $C_{21}H_{18}N_6$, 98%), and 2,5-dihydroxyterephthalaldehyde (Da, $C_8H_6O_4$, 98%) were purchased from Shanghai Haohong Bio-pharmaceutical Technology Co., Ltd. Potassium iodide (KI, 99%) was obtained from Bide Pharmatech Co., Ltd. 2,4,6-Triformylphloroglucinol (Tp, $C_9H_6O_6$, 99%) was provided by Yanshen Technology Co., Ltd. Potassium hydrogen phthalate ($C_8H_5KO_4$, 99%) and urea (CH_4N_2O) were purchased from Aladdin. Acetic acid ($C_2H_4O_2$), dichloromethane (CH_2Cl_2), N, N-dimethylformamide (C_3H_7NO), ethanol (C_2H_5OH), tetrahydrofuran (C_4H_8O), acetone (C_3H_6O, $\geq$99.5%) and methanol (CH_4O) were analytical grade, provided by Tianjin Damao Chemical Reagent. 3-Aminopropyltriethoxysilane (APTS, $C_9H_{23}NO_3Si$, $\geq$98%), 1,2-dichlorobenzene (*o*-DCB, $C_6H_4Cl_2$, $\geq$99%), and 1-butanol (*n*-BuOH, $C_4H_{10}O$, $\geq$99.5%) were purchased from Aladdin. All chemicals were commercially available and used without further purification.

Characterization

The powder XRD pattern was collected on the smart X-ray diffractometer (SmartLab 9 kW, Rigaku, Japan) equipped with Cu Kα radiation (λ = 1.54 Å). FTIR spectroscopy and *in situ* FTIR spectra were recorded on Nicolet iS50 IR spectrometers (Thermo Scientific, USA), and samples were tableted with KBr as support. UV-Vis absorption spectra were recorded on a Hitachi U-3900 UV/VIS spectrophotometer (Hitachi, Japan). SEM was performed on a Quanta250FEG scanning electron microscope (FEI, America). HRTEM images and element mapping were collected on Talos F200 × transmission electron microscopes (FEI, America). UV-Vis DRS measurements were obtained with a Lambda 750 UV/VIS/NIR spectrometer (PerkinElmer, America). EPR spectroscopy was performed on an ESR5000 X-band spectrometer (Bruker Magnettech, Germany). The PL spectra were collected using a F-7000 fluorescence spectrophotometer (Hitachi, Japan). Time-resolved confocal fluorescence microscopy was performed with a Microtime 200 system (PicoQuant, Germany). Contact angle measurements were performed with an SZ-CAMC33 contact angle meter (SZ, China). The isotope of ^{18}O for O_2 was analyzed using an HPR-20 QIC mass spectrometry system (Hiden Analytical, UK).

Synthesis of COF powder

COF powder synthesis followed a procedure reported in the literature.[31] A mixture of TTA (23 mg, 0.085 mmol), TTB (30 mg, 0.085 mmol), *o*-DCB (0.75 mL), *n*-BuOH (0.75 mL), and 6 M aqueous acetic acid (0.1 mL) was added into a Pyrex tube. Then, the tube was sonicated for 15 min, followed by flash freezing at 77 K in a liquid N_2 bath, which was further evacuated to an internal pressure of 50 mTorr and sealed off. The resulting mixture was heated at 120°C for 72 h. After cooling to room temperature, the yellow solid formed was filtered and washed several times with acetone/methanol. Finally, the product was dried at 80°C under vacuum.

Synthesis of COF film

COF film was synthesized via interfacial polymerization at the CH_2Cl_2/water interface according to the following optimized procedure. First, 0.006 mmol of TTB dissolved in 3 mL of CH_2Cl_2 was added to a 20-mL glass bottle. Subsequently, 6 mL deionized water was carefully layered on the CH_2Cl_2 phase to form a two-phase interface. Finally, 0.006 mmol of TTA dissolved in 3 mL of acetic acid (3 M) was slowly added to the topmost layer of the aqueous phase. The reaction system was kept undisturbed at room temperature for 7 days. After the reaction, the film formed at the interface was collected, washed with CH_2Cl_2, N,N-Dimethylformamide (DMF), and ethanol, and dried at room temperature.

Synthesis of NH_2-GO

NH_2-GO was synthesized according to a previous report.[57] 0.1 g of GO was dispersed in 35 mL of deionized water and sonicated for 2 h to obtain a homogeneous dispersion. Then, 0.2 mL APTS was added to the mixture, with stirring for 4 h. After the reaction, the product (NH_2-GO) was collected by centrifugation and thoroughly washed using deionized water for 5 times to remove residual reactants.

Synthesis of COF-[NH_2-GO]

COF-[NH_2-GO] was synthesized via interfacial polymerization at the CH_2Cl_2/water interface according to the following optimized procedure. First, 0.006 mmol of TTB dissolved in 3 mL of CH_2Cl_2 was added to a 20-mL glass bottle. Subsequently, 0.9 mg of NH_2-GO dissolved in 6 mL of deionized water was carefully layered on the CH_2Cl_2 phase to form a two-phase interface. Finally, 0.006 mmol of TTA dissolved in 3 mL of acetic acid (3 M) was slowly added to the topmost layer of the aqueous phase. The reaction system was kept undisturbed at room temperature for 7 days. After the reaction, the film formed at the interface was collected, washed with CH_2Cl_2, DMF, and ethanol, and dried at room temperature.

Synthesis of NH_2-C_3N_4

NH_2-C_3N_4 was synthesized according to a previous report.[58] $N[(CH_2)_2NHCH_2(m\text{-}C_6H_4)CH_2NH(CH_2)_2]_3N$ (12.5 μmol) and urea

(5.0 g) were dissolved in deionized water. The solution was concentrated by heating, and the remaining water was removed by rotary evaporation to obtain a uniform powder. The powder was then transferred to a crucible and pyrolyzed for 2 h under ambient air at 600°C (heating rate: 5°C/min). The product obtained was washed with deionized water and ethanol, and then dried under vacuum at 60°C to obtain light brown powder NH_2-C_3N_4.

Synthesis of COF-[NH_2-C_3N_4]

COF-[NH_2-C_3N_4] was synthesized via interfacial polymerization at the CH_2Cl_2/water interface according to the following optimized procedure. First, 0.006 mmol of TTB dissolved in 3 mL of CH_2Cl_2 was added to a 20-mL glass bottle. Subsequently, 0.9 mg of NH_2-C_3N_4 dissolved in 6 mL deionized water was carefully layered on the CH_2Cl_2 phase to form a two-phase interface. Finally, 0.006 mmol of TTA dissolved in 3 mL of acetic acid (3 M) was slowly added to the topmost layer of the aqueous phase. The reaction system was kept undisturbed at room temperature for 7 days. After the reaction, the film formed at the interface was collected, washed with CH_2Cl_2, DMF, and ethanol, and dried at room temperature.

Synthesis of NH_2-CNT

NH_2-CNT was synthesized from a previous report.[59] COOH-CNT (0.05 g) was dispersed in 50 mL ethanol and ultrasonicated for 30 min. Subsequently, APTS was added to the mixture, then stirred at 70°C for 4 h. After the reaction, the product was washed with water and acetone.

Synthesis of COF-[NH_2-CNT]

COF-[NH_2-CNT] was synthesized via interfacial polymerization at the CH_2Cl_2/water interface according to the following optimized procedure. First, 0.006 mmol of TTB dissolved in 3 mL of CH_2Cl_2 was added to a 20-mL glass bottle. Subsequently, 0.9 mg of NH_2-CNT dissolved in 6 mL deionized water was carefully layered on the CH_2Cl_2 phase to form a two-phase interface. Finally, 0.006 mmol of TTA dissolved in 3 mL of acetic acid (3 M) was slowly added to the topmost layer of the aqueous phase. The reaction system was kept undisturbed at room temperature for 7 days. After the reaction, the film formed at the interface was collected, washed with CH_2Cl_2, DMF, and ethanol, and dried at room temperature.

Synthesis of [TTA-Da-COF]-[NH_2-GO]

[TTA-Da-COF]-[NH_2-GO] was synthesized via interfacial polymerization at the CH_2Cl_2/water interface according to the following optimized procedure. First, 0.006 mmol of Da dissolved in 3 mL CH_2Cl_2 was added to a 20-mL glass bottle. Subsequently, 0.9 mg NH_2-GO dissolved in 6 mL deionized water was carefully layered on the CH_2Cl_2 phase to form a two-phase interface. Finally, 0.006 mmol of TTA dissolved in 3 mL of acetic acid (3 M) was slowly added to the topmost layer of the aqueous phase. The reaction system was kept undisturbed at room temperature for 7 days. After the reaction, the film formed at the interface was collected, washed with CH_2Cl_2, DMF, and ethanol, and dried at room temperature.

Synthesis of [TTA-Tp-COF]-[NH_2-GO]

[TTA-Tp-COF]-[NH_2-GO] was synthesized via interfacial polymerization at the CH_2Cl_2/water interface according to the following optimized procedure. First, 0.006 mmol of Tp dissolved in 3 mL CH_2Cl_2 was added to a 20-mL glass bottle. Subsequently, 0.9 mg of NH_2-GO dissolved in 6 mL deionized water was carefully layered on the CH_2Cl_2 phase to form a two-phase interface. Finally, 0.006 mmol of TTA dissolved in 3 mL of acetic acid (3 M) was slowly added to the topmost layer of the aqueous phase. The reaction system was kept undisturbed at room temperature for 7 days. After the reaction, the film formed at the interface was collected, washed with CH_2Cl_2, DMF, and ethanol, and dried at room temperature.

Photocatalytic test

In a typical experiment, 20 mL deionized water was added to a beaker (r = 2 cm), and the film was placed at the air-water interface. Then, the reaction system was irradiated using a 300 W xenon lamp with a UV cut-off filter ($\lambda > 420$ nm) for 1 h.

H_2O_2 detection methods

The concentration of H_2O_2 was measured by iodimetry. 1 mL of 0.4 M KI aqueous solution and 1 mL of 0.1 M $C_8H_5KO_4$ aqueous solution were added to 1 mL of the reaction solution. The mixture was mixed thoroughly and allowed to stand for 30 min. H_2O_2 reacted with iodine ions (I^-) to form triiodide ions (I_3^-) under acidic conditions, which led to strong absorption near 350 nm. The absorbance at 350 nm was measured by UV-vis spectrophotometer, and the quantity of H_2O_2 was calculated.

COF-[NH_2-GO] film-based device for H_2O_2 photogeneration

To demonstrate practical application, a film-based device was fabricated by integrating the COF-[NH_2-GO] film into a quartz cell equipped with inlet and outlet ports. The setup was irradiated from the top using an Xe lamp. The H_2O_2 solution produced during photocatalysis was collected from the outlet for subsequent antibacterial evaluation.

Sterilization of *E. coli*

The antibacterial efficacy of the obtained H_2O_2 solution was evaluated using the plate colony counting method, with *E. coli*. Initially, a single colony was inoculated into fresh LB medium and incubated on a shaker at 37°C and 200 rpm for 12 h. The initial culture was then diluted 100-fold and further cultured under the same conditions for 3 h to obtain a secondary culture in the logarithmic growth phase (approximately 10^6 CFU/mL). Subsequently, 100 μL of this bacterial suspension was mixed with 500 μL of the obtained H_2O_2 solution and 50 μL $FeSO_4 \cdot 7H_2O$ and incubated for 3 h. The mixtures were then plated, and after incubation at 37°C for 24 h, the colonies were photographed.

Theoretical calculation

All DFT calculations were performed using the Gaussian 16 package.[60] Geometry optimizations were carried out at the B3LYP/def2-SVP level of theory[61] with Grimme's D3 dispersion correction.[62–64] The SMD solvation model[65] employing water as the solvent was applied during all geometry optimizations. Quadratic convergence criteria were used for self-consistent field (SCF) calculations,[66] and the XQC algorithm was invoked when the standard SCF procedure failed to converge. Vibrational frequency analyses were performed under the same conditions as those used for geometry optimization. Single-point energy calculations were subsequently conducted at the M06/def2-TZVP level to obtain more accurate electronic energies.[67] All optimized structures were visualized using CYLview.[68]

Numerical simulations via FEM and PINNs

The governing equations for mass transport read:

$$D_i \nabla^2 c_i + S_i = 0,$$

where *i* stands for different species, *c* for molar concentration, *D* for diffusivity, *S* for the source term (or more specifically, consumption/production rate per unit volume). For both the diphase and triphase systems, the thickness of the diffusion layer was set as 5 mm, and the thickness of the COF film located in between was set to be $h = 5$ μm. At the top boundary for the triphase system, the O_2 partial pressure was assumed to be $p = 0.21$ atm, and the corresponding concentration could be calculated according to the ideal gas law: $c = p/RT$; for the boundaries in aqueous phase, the O_2 concentration was assumed to be 0.27 $\text{mol} \cdot \text{m}^{-3}$ (according to Henry law). The diffusivities were set to be $2.1 \times 10^{-9}\ \text{m}^2\ \text{s}^{-1}$ and $1.5 \times 10^{-9}\ \text{m}^2\ \text{s}^{-1}$ for O_2 and H_2O_2, respectively, in the aqueous/solid phase and $2.1 \times 10^{-5}\ \text{m}^2\ \text{s}^{-1}$ for O_2 in the gas phase. The source terms *S* for the liquid and gas phases were set as 0 and calculated according to $S_i = J_i/h$ for the solid phase, where J_i is the experimentally determined consumption/production rate per unit area (unit, $\text{mol}\ \text{m}^{-2}\ \text{s}^{-1}$). At the air-solid interface, the Henry constant of 0.032 was set for O_2. At the interfaces between the liquid/solid/gas phases, proper boundary conditions regarding the continuities of chemical potentials and transport fluxes were prescribed.

For the FEM, a uniform mesh of 5 mm and a quadratic shape function were used. For the PINNs, three networks (each for a liquid, solid, or gas phase) with two hidden layers (each with 32 neurons) were used; the activation functions were set as hyperbolic tangent for the hidden layers and linear for the output layer. Wherever a Dirichlet boundary condition was prescribed, a hard constraint was implemented. Mean square error losses were used to monitor the numerical residuals for the governing equation as well as the continuities of chemical potentials and transport fluxes at the liquid/solid/gas interfaces; the weights for different losses were dynamically adjusted during training. For each network, an Adam (Adaptive Momentum) optimizer was employed with a learning rate of 0.001.

RESOURCE AVAILABILITY

Lead contact

Further information and requests for resources and reagents should be directed to and will be fulfilled by the lead contact, Kuo Yuan (yuankuo@email.tjut.edu.cn).

Materials availability

This study did not generate new, unique reagents.

Data and code availability

The data and code associated with the study have not been deposited in a public repository but are available from the lead contact upon reasonable request.

ACKNOWLEDGMENTS

This work was supported by the National Natural Science Foundation of China (22575173, 22205162, 22571228, 22531007, 22271218, 22201209, and 22571227) and the Natural Science Foundation of Tianjin (nos. 24JCZDJC00220, 25JCQNJC00150, and 25JCQNJC00480).

AUTHOR CONTRIBUTIONS

Y.L. conducted the experiments and prepared the first draft of the manuscript; Y.Z. revised and polished the manuscript, characterized films, and analyzed experimental data; W.S. conducted the theoretical calculation; C.Z. conducted numerical simulations and physics-informed neural networks; Q.Y. revised the manuscript; Z.L. revised the supporting information; F.Y. and J.G. conducted the sterilization of *E. coli*; Q.Y. provided help in numerical simulations; W.L. and M.W. helped determine the crystal structures of COFs; X.Z. supported spectrum characterization; W.H. revised the film characterization part in the manuscript; K.Y. provided the idea of Janus film photocatalyst, finished the preparation of manuscript and supporting information, and supervised this work; D.Z. provided suggestion for photocatalysis; and T.L. revised the manuscript.

DECLARATION OF INTERESTS

The authors declare no competing interests.

SUPPLEMENTAL INFORMATION

Supplemental information can be found online at https://doi.org/10.1016/j.matt.2026.102679.

Received: December 21, 2025
Revised: January 27, 2026
Accepted: January 29, 2026

REFERENCES

1. Teng, Z., Zhang, Q., Yang, H., Kato, K., Yang, W., Lu, Y.R., Liu, S., Wang, C., Yamakata, A., Su, C., et al. (2021). Atomically dispersed antimony on carbon nitride for the artificial photosynthesis of hydrogen peroxide. Nat. Catal. *4*, 374–384. https://doi.org/10.1038/s41929-021-00605-1.
2. Hou, H., Zeng, X., and Zhang, X. (2020). Production of Hydrogen Peroxide by Photocatalytic Processes. Angew. Chem. Int. Ed. *59*, 17356–17376. https://doi.org/10.1002/anie.201911609.
3. Sun, Y., Han, L., and Strasser, P. (2020). A comparative perspective of electrochemical and photochemical approaches for catalytic H_2O_2 production. Chem. Soc. Rev. *49*, 6605–6631. https://doi.org/10.1039/d0cs00458h.
4. Liu, Y., Guo, Y., Sathishkumar, N., Liu, M., Li, L., Sang, Z., Feng, R., Sun, Z., Sun, C., Luo, M., et al. (2025). Halogen atom-induced local asymmetric electron in covalent organic frameworks boosts photosynthesis of hydrogen peroxide from water and air. Matter *8*, 102076. https://doi.org/10.1016/j.matt.2025.102076.
5. Campos-Martin, J.M., Blanco-Brieva, G., and Fierro, J.L.G. (2006). Hydrogen Peroxide Synthesis: An Outlook beyond the Anthraquinone Process. Angew. Chem. Int. Ed. *45*, 6962–6984. https://doi.org/10.1002/anie.200503779.
6. Tan, H., Zhou, P., Liu, M., Zhang, Q., Liu, F., Guo, H., Zhou, Y., Chen, Y., Zeng, L., Gu, L., et al. (2023). Photocatalysis of water into hydrogen

peroxide over an atomic Ga-N_5 site. Nat. Synth. *2*, 557–563. https://doi.org/10.1038/s44160-023-00272-z.

7. Liu, R., Chen, Y., Yu, H., Položij, M., Guo, Y., Sum, T.C., Heine, T., and Jiang, D. (2024). Linkage-engineered donor–acceptor covalent organic frameworks for optimal photosynthesis of hydrogen peroxide from water and air. Nat. Catal. *7*, 195–206. https://doi.org/10.1038/s41929-023-01102-3.
8. Liang, C.-P., Huang, J.-R., Zhu, H.-L., Zhao, Z.-H., Yu, C., Liao, P.-Q., and Chen, X.-M. (2024). Precisely Tailoring the First Coordination Shell of Metal Centers in Porous Nitrogen-Doped Carbon Promoting Electroreduction of CO_2 Under Neutral Condition. CCS Chem. *6*, 1978–1986. https://doi.org/10.31635/ccschem.023.202303333.
9. Krishnaraj, C., Sekhar Jena, H., Bourda, L., Laemont, A., Pachfule, P., Roeser, J., Chandran, C.V., Borgmans, S., Rogge, S.M.J., Leus, K., et al. (2020). Strongly Reducing (Diarylamino)benzene-Based Covalent Organic Framework for Metal-Free Visible Light Photocatalytic H_2O_2 Generation. J. Am. Chem. Soc. *142*, 20107–20116. https://doi.org/10.1021/jacs.0c09684.
10. Bai, C.-W., Liu, L.-L., Chen, J.-J., Chen, F., Zhang, Z.-Q., Sun, Y.-J., Chen, X.-J., Yang, Q., and Yu, H.-Q. (2024). Circumventing bottlenecks in H_2O_2 photosynthesis over carbon nitride with iodine redox chemistry and electric field effects. Nat. Commun. *15*, 4718. https://doi.org/10.1038/s41467-024-49046-x.
11. Zhang, L., Chen, Z., Li, X.X., Wang, X., Gu, Q., Zheng, Z., Aratani, N., Lee, C.S., Lan, Y.Q., and Zhang, Q. (2025). Constructing Dual-Functional Organic Cuboctahedron Cages with Two Different Triangular Building Units for Efficient Artificial Photosynthesis of Hydrogen Peroxide from Water and Oxygen. J. Am. Chem. Soc. *147*, 27847–27854. https://doi.org/10.1021/jacs.5c06974.
12. Yang, B., Hou, M., and Gao, S. (2025). Total Synthesis of Polycyclic Natural Products via Photoenolization/Diels-Alder Reaction. Acc. Chem. Res. *58*, 1308–1322. https://doi.org/10.1021/acs.accounts.5c00084.
13. Liu, Y.C., Huang, J.R., Zhu, H.L., Qiu, X.F., Yu, C., Chen, X.M., and Liao, P.Q. (2025). Electrosynthesis of pure urea from pretreated flue gas in a proton-limited environment established in a porous solid-state electrolyte electrolyser. Nat. Nanotechnol. *20*, 907–913. https://doi.org/10.1038/s41565-025-01914-3.
14. Sun, M., Wang, X., Li, Y., Pan, H., Murugananthan, M., Han, Y., Wu, J., Zhang, M., Zhang, Y., and Kang, Z. (2022). Bifunctional Pd-Ox Center at the Liquid–Solid–Gas Triphase Interface for H_2O_2 Photosynthesis. ACS Catal. *12*, 2138–2149. https://doi.org/10.1021/acscatal.1c05324.
15. Chang, J.N., Li, Q., Shi, J.W., Zhang, M., Zhang, L., Li, S., Chen, Y., Li, S.L., and Lan, Y.Q. (2023). Oxidation-Reduction Molecular Junction Covalent Organic Frameworks for Full Reaction Photosynthesis of H_2O_2. Angew. Chem. Int. Ed. *62*, e202218868. https://doi.org/10.1002/anie.202218868.
16. Liu, C., Liu, X., Chen, B., Li, Z., Ou, X., Lu, Y., Liu, Y., Wu, C., Yao, S., Liu, Y., et al. (2025). Squaric acid-based zwitterionic covalent organic framework induces triple synergy for boosted hydrogen peroxide photosynthesis. Nat. Commun. *16*, 8941. https://doi.org/10.1038/s41467-025-63997-9.
17. Qu, S., Wu, H., and Ng, Y.H. (2023). Clean Production of Hydrogen Peroxide: A Heterogeneous Solar-Driven Redox Process. Adv. Energy Mater. *13*, 2301047. https://doi.org/10.1002/aenm.202301047.
18. Guo, Y., Dong, Y., Liu, B., Ni, B., Pan, C., Zhang, J., Zhao, H., Wang, G., and Zhu, Y. (2024). Effective H_2O_2 Photosynthesis in Gas-Liquid-Solid Triphase System with Self-Floating Conjugated Organic Polymers. Adv. Funct. Mater. *34*, 2402920. https://doi.org/10.1002/adfm.202402920.
19. Ling, H., Sun, H., Lu, L., Zhang, J., Liao, L., Wang, J., Zhang, X., Lan, Y., Li, R., Lu, W., et al. (2024). Sustainable photocatalytic hydrogen peroxide production over octonary high-entropy oxide. Nat. Commun. *15*, 9505. https://doi.org/10.1038/s41467-024-53896-w.
20. Zhi, Q., Liu, W., Jiang, R., Zhan, X., Jin, Y., Chen, X., Yang, X., Wang, K., Cao, W., Qi, D., and Jiang, J. (2022). Piperazine-Linked Metalphthalocyanine Frameworks for Highly Efficient Visible-Light-Driven H_2O_2 Photosynthesis. J. Am. Chem. Soc. *144*, 21328–21336. https://doi.org/10.1021/jacs.2c09482.
21. Yan, S., Li, Y., Yang, X., Jia, X., Xu, J., and Song, H. (2024). Photocatalytic H_2O_2 Generation Reaction with a Benchmark Rate at Air-Liquid-Solid Joint Interfaces. Adv. Mater. *36*, 2307967. https://doi.org/10.1002/adma.202307967.
22. Qiao, C., Xian, W., Lai, Z., Huang, Z., Guo, Q., Wang, S., Dai, Z., Xiong, Y., Meng, X., Ma, S., and Sun, Q. (2025). Covalent Organic Framework Membranes with Asymmetric Wettability for Efficient Photocatalytic H_2O_2 Synthesis. Angew. Chem. Int. Ed. *64*, e202519513. https://doi.org/10.1002/anie.202519513.
23. Bai, R., Niu, J., Zhang, X., Li, Q., Dong, C., Shen, Q., Xue, J., and Zhu, Y. (2025). Enhanced photocatalytic CO_2 reduction in floatable CMF/Bi_2WO_6/C_3N_4 gas-liquid-solid three-phase heterojunction system. Appl. Catal. B Environ. *374*, 125395. https://doi.org/10.1016/j.apcatb.2025.125395.
24. Zhang, W., Tan, Q., Liu, T., He, Y., Chen, G., Chen, K., Han, D., Qin, D., and Niu, L. (2023). Fabrication of water-floating litchi-like polystyrene-sphere-supported TiO_2/Bi_2O_3 S-scheme heterojunction for efficient photocatalytic degradation of tetracycline. Mater. Horiz. *10*, 5869–5880. https://doi.org/10.1039/d3mh01348k.
25. Li, L., Xu, L., Hu, Z., and Yu, J.C. (2021). Enhanced Mass Transfer of Oxygen through a Gas-Liquid-Solid Interface for Photocatalytic Hydrogen Peroxide Production. Adv. Funct. Mater. *31*, 2106120. https://doi.org/10.1002/adfm.202106120.
26. Sheng, X., Liu, Z., Zeng, R., Chen, L., Feng, X., and Jiang, L. (2017). Enhanced Photocatalytic Reaction at Air-Liquid-Solid Joint Interfaces. J. Am. Chem. Soc. *139*, 12402–12405. https://doi.org/10.1021/jacs.7b07187.
27. Li, Y., Pei, Z., Luan, D., and Lou, X.W.D. (2024). Triple-Phase Photocatalytic H_2O_2 Production on a Janus Fiber Membrane with Asymmetric Hydrophobicity. J. Am. Chem. Soc. *146*, 3343–3351. https://doi.org/10.1021/jacs.3c12465.
28. Jiang, D., Tan, V.G.W., Gong, Y., Shao, H., Mu, X., Luo, Z., and He, S. (2025). Semiconducting Covalent Organic Frameworks. Chem. Rev. *125*, 6203–6308. https://doi.org/10.1021/acs.chemrev.4c00950.
29. Yong, Z., and Ma, T. (2023). Solar-to-H_2O_2 Catalyzed by Covalent Organic Frameworks. Angew. Chem. Int. Ed. *62*, e202308980. https://doi.org/10.1002/anie.202308980.
30. Rodriguez-Camargo, A., Endo, K., and Lotsch, B.V. (2024). Celebrating Ten Years of Covalent Organic Frameworks for Solar Energy Conversion: Past, Present and Future. Angew. Chem. Int. Ed. *63*, e202413096. https://doi.org/10.1002/anie.202413096.
31. Das, P., Chakraborty, G., Roeser, J., Vogl, S., Rabeah, J., and Thomas, A. (2023). Integrating Bifunctionality and Chemical Stability in Covalent Organic Frameworks via One-Pot Multicomponent Reactions for Solar-Driven H_2O_2 Production. J. Am. Chem. Soc. *145*, 2975–2984. https://doi.org/10.1021/jacs.2c11454.
32. Chen, H., Jena, H.S., Feng, X., Leus, K., and Van Der Voort, P. (2022). Engineering Covalent Organic Frameworks as Heterogeneous Photocatalysts for Organic Transformations. Angew. Chem. Int. Ed. *61*, e202204938. https://doi.org/10.1002/anie.202204938.
33. Côté, A.P., Benin, A.I., Ockwig, N.W., O'Keeffe, M., Matzger, A.J., and Yaghi, O.M. (2005). Porous, Crystalline, Covalent Organic Frameworks. Science *310*, 1166–1170. https://doi.org/10.1126/science.1120411.
34. Song, Y., Hou, L., Lan, P.C., Xing, Z., Sun, Q., Lv, J., Li, J., Zhang, D., Dai, Z., AlShahrani, T., and Ma, S. (2025). Creating electrochemical accessibility in covalent organic frameworks for uranium extraction via electrodeposition. Nat. Commun. *16*, 7093. https://doi.org/10.1038/s41467-025-62501-7.
35. Dey, A., Chakraborty, S., Singh, A., Rahimi, F.A., Biswas, S., Mandal, T., and Maji, T.K. (2024). Microwave Assisted Fast Synthesis of a Donor-Acceptor COF Towards Photooxidative Amidation Catalysis. Angew. Chem. Int. Ed. *63*, e202403093. https://doi.org/10.1002/anie.202403093.

Please cite this article in press as: Li et al., Self-floating COF-based Janus film: A robust triphase interface boosting charge separation for efficient H_2O_2 photosynthesis, Matter (2026), https://doi.org/10.1016/j.matt.2026.102679

36. Guo, S., Zhao, K., Liang, L., Li, Z., Han, B., Ou, X., Yao, S., Lin, Z., Dong, Z., Liu, Y., et al. (2025). Fully Conjugated Sp^2 Carbon-Linked Covalent Organic Frameworks Enables Accelerated Exciton Process for Superior Singlet Oxygen Photosynthesis for Water Remediation. Angew. Chem. Int. Ed. *64*, e202509141. https://doi.org/10.1002/anie.202509141.
37. Hu, X., Zhan, Z., Zhang, J., Hussain, I., and Tan, B. (2021). Immobilized covalent triazine frameworks films as effective photocatalysts for hydrogen evolution reaction. Nat. Commun. *12*, 6596. https://doi.org/10.1038/s41467-021-26817-4.
38. Ghosh, S., Küçükkeçeci, H., Paitandi, R.P., Weigelt, V., Dippold, V., Seki, S., and Thomas, A. (2024). Low band gap semiconducting covalent organic framework films with enhanced photocatalytic hydrogen evolution. J. Mater. Chem. A *12*, 247–255. https://doi.org/10.1039/d3ta04552h.
39. Huang, D.S., Wang, Y., Tang, Y., Huang, J.R., Li, P.X., Liang, C.P., Zhao, Z.H., Liao, P.Q., and Chen, X.M. (2025). Embedding a self-supporting MOF-based molecular sieve membrane into an electrolyzer for boosting electroreduction of CO_2 in air and flue gas to HCOOH. Natl. Sci. Rev. *12*, nwaf329. https://doi.org/10.1093/nsr/nwaf329.
40. Kumar Mahato, A., Bag, S., Sasmal, H.S., Dey, K., Giri, I., Linares-Moreau, M., Carbonell, C., Falcaro, P., Gowd, E.B., Vijayaraghavan, R.K., and Banerjee, R. (2021). Crystallizing Sub 10 nm Covalent Organic Framework Thin Films via Interfacial–Residual Concomitance. J. Am. Chem. Soc. *143*, 20916–20926. https://doi.org/10.1021/jacs.1c09740.
41. Sasmal, H.S., Halder, A., Kunjattu H, S., Dey, K., Nadol, A., Ajithkumar, T.G., Ravindra Bedadur, P., and Banerjee, R. (2019). Covalent Self-Assembly in Two Dimensions: Connecting Covalent Organic Framework Nanospheres into Crystalline and Porous Thin Films. J. Am. Chem. Soc. *141*, 20371–20379. https://doi.org/10.1021/jacs.9b10788.
42. Khan, N.A., Zhang, R., Wu, H., Shen, J., Yuan, J., Fan, C., Cao, L., Olson, M.A., and Jiang, Z. (2020). Solid-Vapor Interface Engineered Covalent Organic Framework Membranes for Molecular Separation. J. Am. Chem. Soc. *142*, 13450–13458. https://doi.org/10.1021/jacs.0c04589.
43. Wu, T., Qian, Y., Zhu, Z., Yu, W., Zhang, L., Liu, J., Shen, X., Zhou, X., Qian, T., and Yan, C. (2025). Imine-Linked 3D Covalent Organic Framework Membrane Featuring Highly Charged Sub-1 nm Channels for Exceptional Lithium-Ion Sieving. Adv. Mater. *37*, 2415509. https://doi.org/10.1002/adma.202415509.
44. Mahato, A.K., Paul, S., and Banerjee, R. (2025). Synthesis innovations for crystallizing covalent organic framework thin films on biological and non-biological substrates. Chem. Soc. Rev. *54*, 3578–3598. https://doi.org/10.1039/d4cs01222d.
45. Yadav, D., Kumar, A., Kim, J.Y., Park, N.-J., and Baeg, J.-O. (2021). Interfacially synthesized 2D COF thin film photocatalyst: efficient photocatalyst for solar formic acid production from CO_2 and fine chemical synthesis. J. Mater. Chem. A *9*, 9573–9580. https://doi.org/10.1039/d1ta00802a.
46. Chen, Y., Liu, R., Guo, Y., Wu, G., Sum, T.C., Yang, S.W., and Jiang, D. (2024). Hierarchical assembly of donor-acceptor covalent organic frameworks for photosynthesis of hydrogen peroxide from water and air. Nat. Synth. *3*, 998–1010. https://doi.org/10.1038/s44160-024-00542-4.
47. Gong, Y.N., Mei, J.H., Shi, W.J., Liu, J.W., Zhong, D.C., and Lu, T.B. (2024). Boosting CO_2 Photoreduction to Formate or CO with High Selectivity over a Covalent Organic Framework Covalently Anchored on Graphene Oxide. Angew. Chem. Int. Ed. *63*, e202318735. https://doi.org/10.1002/anie.202318735.
48. Zhao, Y., Zhang, Y., Wang, L., Ai, C., and Zhang, J. (2025). Efficient H_2O_2 production coupling Rhodamine B degradation over covalent organic framework/g-C_3N_4 with S-scheme charge separation mechanism and fully hole-electron utilization ability. J. Mater. Sci. Technol. *229*, 213–222. https://doi.org/10.1016/j.jmst.2024.12.040.
49. Yang, Y., Liu, J., Gu, M., Cheng, B., Wang, L., and Yu, J. (2023). Bifunctional TiO_2/COF S-scheme photocatalyst with enhanced H_2O_2 production and furoic acid synthesis mechanism. Appl. Catal. B Environ. *333*, 122780. https://doi.org/10.1016/j.apcatb.2023.122780.
50. Yuan, K., Liu, Z., Yan, Z., Yun, Q., Song, T., Guo, J., Zhang, X., Zhong, D., Tang, Z., Lu, T., and Hu, W. (2024). Metal-Organic Framework-Based Hetero-Phase Nanostructure Photocatalysts with Molecular-Scale Tunable Energy Levels. Angew. Chem. Int. Ed. *63*, e202402693. https://doi.org/10.1002/anie.202402693.
51. Zhou, J., Chen, J., Li, N., Gou, F., Yang, Z., Zeng, M., and Shao, M. (2025). Covalent Organic Frameworks with Constrained Palladium Nanoclusters Lock the Enol-Keto Tautomerism Enhancing Hydrogen Peroxide Photosynthesis. Small *21*, 2409006. https://doi.org/10.1002/smll.202409006.
52. Zhang, F., Lv, X., Wang, H., Cai, J., Wang, H., Bi, S., Wei, R., Yang, C., Zheng, G., and Han, Q. (2025). p-π Conjugated Covalent Organic Frameworks Expedite Molecular Triplet Excitons for H_2O_2 Production Coupled with Biomass Upgrading. Adv. Mater. *37*, 2502220. https://doi.org/10.1002/adma.202502220.
53. Kong, X., Wu, Z., Strømme, M., and Xu, C. (2023). Ambient Aqueous Synthesis of Imine-Linked Covalent Organic Frameworks (COFs) and Fabrication of Freestanding Cellulose Nanofiber@COF Nanopapers. J. Am. Chem. Soc. *146*, 742–751. https://doi.org/10.1021/jacs.3c10691.
54. Laemont, A., Matthys, G., Lavendomme, R., and Van Der Voort, P. (2024). Mild and Scalable Conditions for the Solvothermal Synthesis of Imine-Linked Covalent Organic Frameworks. Angew. Chem. Int. Ed. *63*, e202412420. https://doi.org/10.1002/anie.202412420.
55. Tian, Q., Zeng, X.K., Zhao, C., Jing, L.Y., Zhang, X.W., and Liu, J. (2023). Exceptional Photocatalytic Hydrogen Peroxide Production from Sandwich-Structured Graphene Interlayered Phenolic Resins Nanosheets with Mesoporous Channels. Adv. Funct. Mater. *33*, 2213173. https://doi.org/10.1002/adfm.202213173.
56. Wang, W., Chen, Z., Li, C., Cheng, B., Yang, K., Zhang, S., Luo, G., Yu, J., and Cao, S. (2025). Graphene Quantum Dot-Modified $Mn_{0.2}Cd_{0.8}S$ for Efficient Overall Photosynthesis of H_2O_2. Adv. Funct. Mater. *35*, 2422307. https://doi.org/10.1002/adfm.202422307.
57. Yan, J.M., Li, S.J., Yi, S.S., Wulan, B.R., Zheng, W.T., and Jiang, Q. (2018). Anchoring and Upgrading Ultrafine NiPd on Room-Temperature-Synthesized Bifunctional NH_2-N-rGO toward Low-Cost and Highly Efficient Catalysts for Selective Formic Acid Dehydrogenation. Adv. Mater. *30*, 1703038. https://doi.org/10.1002/adma.201703038.
58. Tao, K.-Y., Yuan, K., Yang, W., Zhong, D.-C., and Lu, T.-B. (2023). A template co-pyrolysis strategy towards the increase of amino/imino content within g-C_3N_4 for efficient CO_2 photoreduction. Chem. Eng. J. *455*, 140630. https://doi.org/10.1016/j.cej.2022.140630.
59. Kathi, J., and Rhee, K.Y. (2007). Surface modification of multi-walled carbon nanotubes using 3-aminopropyltriethoxysilane. J. Mater. Sci. *43*, 33–37. https://doi.org/10.1007/s10853-007-2209-2.
60. Frisch, M.J., Trucks, G.W., Schlegel, H.B., Scuseria, G.E., Robb, M.A., Cheeseman, J.R., Scalmani, G., Barone, V., Petersson, G.A., and Nakatsuji, H. (2016). Gaussian 16 (Gaussian, Inc.).
61. Becke, A. (1993). Density-functional thermochemistry. III. The role of exact exchange. J. Chem. Phys. *98*, 5648.
62. Grimme, S. (2006). Semiempirical GGA-type density functional constructed with a long-range dispersion correction. J. Comput. Chem. *27*, 1787–1799. https://doi.org/10.1002/jcc.20495.
63. Grimme, S., Antony, J., Ehrlich, S., and Krieg, H. (2010). A consistent and accurate ab initio parametrization of density functional dispersion correction (DFT-D) for the 94 elements H-Pu. J. Chem. Phys. *132*, 154104. https://doi.org/10.1063/1.3382344.
64. Grimme, S., Ehrlich, S., and Goerigk, L. (2011). Effect of the damping function in dispersion corrected density functional theory. J. Comput. Chem. *32*, 1456–1465. https://doi.org/10.1002/jcc.21759.
65. Marenich, A.V., Cramer, C.J., and Truhlar, D.G. (2009). Universal Solvation Model Based on Solute Electron Density and on a Continuum Model of the

Solvent Defined by the Bulk Dielectric Constant and Atomic Surface Tensions. J. Phys. Chem. B *113*, 6378–6396. https://doi.org/10.1021/jp810292n.

66. Miertuš, S., Scrocco, E., and Tomasi, J. (1981). Electrostatic interaction of a solute with a continuum. A direct utilizaion of AB initio molecular potentials for the prevision of solvent effects. Chem. Phys. *55*, 117–129. https://doi.org/10.1016/0301-0104(81)85090-2.

67. Zhao, Y., and Truhlar, D.G. (2008). The M06 suite of density functionals for main group thermochemistry, thermochemical kinetics, noncovalent interactions, excited states, and transition elements: two new functionals and systematic testing of four M06-class functionals and 12 other functionals. Theor. Chem. Acc. *120*, 215–241. https://doi.org/10.1007/s00214-007-0310-x.

68. Legault, C.Y. (2009). CYLview. http://www.cylview.org.